ELSEVIER

Journal of Fluids and Structures 23 (2007) 839–857

JOURNAL OF FLUIDS AND STRUCTURES

www.elsevier.com/locate/jfs

Immersed finite element method for fluid-structure interactions

L.T. Zhang*, M. Gay

Department of Mechanical, Aerospace, and Nuclear Engineering, Rensselaer Polytechnic Institute, Troy, NY 12180, USA

Received 23 March 2006; accepted 20 January 2007
Available online 18 May 2007

Abstract

In this paper, we present a detailed derivation of the numerical method, Immersed Finite Element Method (IFEM), for the solution of fluid-structure interaction problems. This method is developed based on the Immersed Boundary (IB) method that was initiated by Peskin, with additional capabilities in handling nonuniform and independent meshes and applying arbitrary boundary conditions on both fluid and solid domains. A higher order interpolation function is adopted from one of the mesh-free methods, the Reproducing Kernel Particle Method (RKPM), which relieves the uniformity constraint of fluid meshes. Two 2-D example problems are presented to illustrate the capabilities of the algorithm. The accuracy in the numerical analysis demonstrates that the IFEM algorithm is a reliable and robust numerical approach to solve fluid and deformable solid interactions.

Keywords: Immersed finite element method; Fluid-structure interactions; Immersed boundary method; Reproducing kernel particle method

1. Introduction

Numerical investigations of fluid-structure interaction type problems require reliable numerical modeling and simulation tools. An efficient and robust modeling technique is essential in studying complicated physical phenomena, especially in the bioscience and biomedical fields. In the past few decades, numerous research efforts have been directed to method development for fluid-structure interactions. Methods developed by Tezduyar et al. (1992), Johnson and Texduyar (1995, 1997, 1999), are widely used in he simulation of fluid-particle and fluid-structure interactions, such as the studies on parachute aerodynamics (Stein et al., 2001). The Arbitrary Lagrangian Eulerian (ALE) numerical approach used by Hughes et al. (1981), Liu (1981), Liu and Ma (1982), Huerta and Liu (1988), Liu et al. (1988), Hu et al. (2001), and Zhang et al. (2003), is another technique to accommodate the complicated fluid-structure interface. Nevertheless, mesh updating or remeshing processes can be computationally expensive for the ALE algorithm. Belytschko and Kennedy (1976), Belytschko (1980), Belytschko et al. (1980), Belytschko and Mullen (1981), Liu et al. (1986) used numerical modeling to conduct fluid-structure impact analyses. Fortin and Glowinski (1983), Glowinski et al. (1999, 2001) developed the Distributed Lagrange Multiplier method to study particulate flows. Recently,

*Corresponding author.
E-mail address: ZhangLucy@rpi.edu (L.T. Zhang).

0889-9746/$ - see front matter © 2007 Published by Elsevier Ltd.
doi:10.1016/j.jfluidstructs.2007.01.001

Nomenclature

Fluid variables

$\mathbf{f}^{EXT}$	external force applied
$\mathbf{f}^{FSI}$	interaction force
ρ	density
$\mathbf{x}$	grid position
$\mathbf{v}$	velocity
$\boldsymbol{\sigma}$	Cauchy stress

Solid variables

$\mathbf{f}^{EXT,s}$	external force applied
$\mathbf{f}^{FSI,s}$	interaction force
ρ^s	density
$\mathbf{x}^s$	current position
$\mathbf{v}^s$	velocity
$\mathbf{a}^s$	acceleration
$\mathbf{u}^s$	displacement
$\mathbf{X}^s$	initial position
$\boldsymbol{\sigma}^s$	Cauchy stress

researchers have applied the eXtended Finite Element Method (XFEM) to study fluid-structure interactions (Wagner et al., 2001; Chessa et al., 2002; Chessa and Belytschko, 2003).

Among the computational methods developed for fluid-structure interactions, one of the most noticeable contributions was from Peskin (1977) who developed the Immersed Boundary (IB) method to study the blood flow around heart valves (Peskin, 1972, 1977; McCracken and Peskin, 1980; McQueen and Peskin, 1983; Peskin and McQueen, 1989, 1990, 1991, 1992, 1993, 1994, 1995, 1996; McQueen and Peskin, 2001). The mathematical formulation of the IB method employs a mixture of Eulerian and Lagrangian descriptions for fluid and solid domains. The interaction between fluid and structure is accomplished by distributing nodal forces and interpolating nodal velocities between the Eulerian and Lagrangian domains through a smoothed approximation of the Dirac delta function. The advantage of the IB method is that the fluid-structure interface is tracked automatically, which circumvents costly mesh updating algorithms. One major obstacle of the IB method, however, is the assumption of the fiber-like immersed elastic structure. This assumption restrains realistic modeling of structures that may require complicated constitutive laws and an accurate representation of the finite volume they occupy within the fluid domain. Nevertheless, the IB method made great contributions in the computational field; it paved the way for future scientists and engineers to employ and take the numerical computing technology to a new level.

The goal of this paper is to present a detailed derivation and evaluation of a novel numerical algorithm, named Immersed Finite Element Method (IFEM), for the solutions of fluid-structure interaction problems (Liu et al., 2004a, b; Y. Liu, 2006; Gay et al., 2006; Liu et al., 2006). This algorithm is built based on the fundamental concept of IB method, but eliminated the aforementioned drawbacks of the IB method by adopting features of the Extended Immersed Boundary Method (EIBM) developed by Wang and Liu (2004). The IFEM also relies on the delta function properties that are commonly used as the shape functions in mesh-free methods (Liu et al., 1996a, b; Li and Liu, 1996, 1999, 2002, 2004), such as the Reproducing Kernel Particle Method (Liu et al., 1995; Liu and Chen, 1995; Zhang et al., 2002). This mesh-free delta function provides not only a higher order smoothness in the coupling procedures used between fluid and solid domains, but also the ability to handle nonuniform fluid grids, which offers flexibility and robustness in the numerical scheme. The basic concepts of the IFEM are illustrated in Zhang et al. (2004). However, it lacks the detailed derivations and accuracy analysis of the method. This paper presents the complete formulation and comprehensive explanations and analysis of this IFEM approach.

The outline of this paper is as follows. The equations of motion are first derived in Section 2 with detailed kinematics and governing equations of fluid and solid, as well as the interaction interpolations. Two verification examples are presented in Section 3. The first is a soft disk falling in a channel where the terminal velocity of the disk can be compared with an analytical solution obtained for a rigid disk. The second example shows the motion of a thin leaflet driven by a sinusoidal flow. Both examples are presented to demonstrate the main features, capabilities and efficiency of the IFEM. Finally, conclusions are drawn in Section 4.

2. Equations of motion

The primary goal of this section is to derive and introduce the equations of motion for the Immersed Finite Element Method algorithm. For brevity and clear understanding of the concept, we start the derivation from the principle of virtual work or the weak form. The weak forms of the derived equations are equivalent to their strong forms if the weak form solution is smooth enough to satisfy at least C^0 continuity.

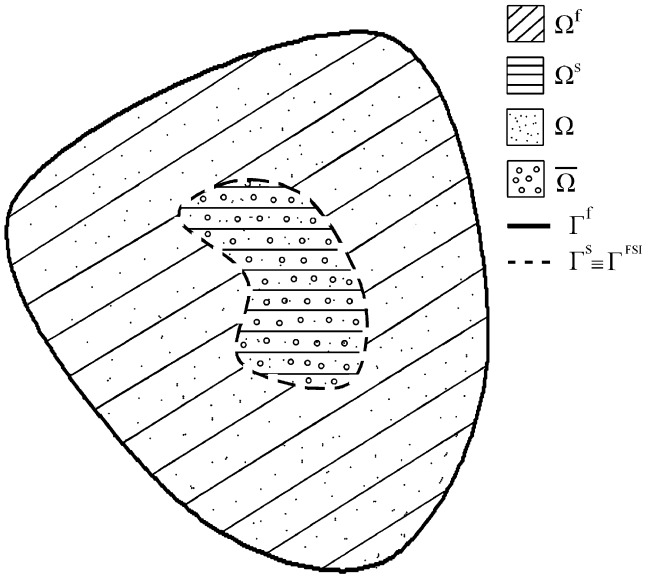

Fig. 1. Computational domain decomposition.

2.1. Kinematics

Let us consider a deformable structure that occupies a finite domain, Ω^s, which is completely immersed in a fluid domain Ω^f, as illustrated in Fig. 1. The fluid and the solid together occupy the entire computational domain Ω, and they intersect at a common interface Γ^{FSI}, where FSI stands for fluid-structure interface (i.e., $\Omega^f \cup \Omega^s = \Omega$ and $\Omega^f \cap \Omega^s = \Gamma^{FSI}$). The FSI represents a line if Ω is a two-dimensional domain or a surface if Ω is in three-dimensions. The interface Γ^{FSI} coincides with the solid boundary Γ^s. The nomenclature involved can be partitioned into two categories: one belongs to the solid and the other to the fluid. The notations associated with the solid have superscript s to distinguish them from those of the fluid.

2.2. The overlapping domain

We first assume that the fluid exists everywhere in the domain, Ω. This assumption allows us to generate fluid and solid meshes and solve fluid and solid equations independently, thus avoiding frequent mesh updating schemes required to track the fluid-structure interface. In the IFEM, the solid immersed in the fluid domain occupies a physical space or volume in the computational domain. Therefore, when the solid domain, Ω^s, is constructed, it overlaps with the entire domain Ω filled with fluid. Since both the solid and the "artificial" fluid coexist in the solid domain, Ω^s, we name it the "overlapping domain", $\bar{\Omega}$, i.e., $\Omega^s \equiv \bar{\Omega}$. This assumption may simplify the computations, but does not comply with the actual physics. Therefore, this "artificial" fluid effect in the solid domain must be eliminated when formulating the equations of motion.

Another important assumption is that the interface between the fluid and the solid must abide by the no-slip boundary condition. Therefore, the solid structure follows wherever the artificial fluid goes, or it can be thought of as the artificial fluid movement being induced by the forces generated by the solid.

To better illustrate and explain the equations to be formulated for this overlapping domain, we start by deriving the principle of virtual work for the solid domain with a test function, $\boldsymbol{\delta v}^s$,

$$\int_{\Omega^s} \delta v_i^s \left[\rho^s \frac{\mathrm{d}v_i^s}{\mathrm{d}t} - \sigma_{ij,j}^s - f_i^{\mathrm{EXT},s} \right] \mathrm{d}\Omega = 0. \tag{1}$$

The terms in the bracket of Eq. (1) describe the governing equation for the solid, where $\boldsymbol{\sigma}^s$ is the stress which is directly related to the internal force. The term $\rho^s(\mathrm{d}v_i^s/\mathrm{d}t)$, or $\rho^s \ddot{u}^s$, is the inertial force and $\mathbf{f}^{\mathrm{EXT},s}$ is the applied external force, such as gravity.

We now want to rewrite Eq. (1) so that the terms related to the artificial fluid are included without contradicting equilibrium. Assuming there is no external force applied to the fluid domain, Eq. (1) becomes

$$\int_{\Omega^s} \delta v_i^s \left[(\rho^s - \underline{\rho}) \frac{\mathrm{d}v_i^s}{\underline{\mathrm{d}t}} + \rho \underline{\frac{\mathrm{d}v_i^s}{\mathrm{d}t}} - (\sigma_{ij,j}^s - \underline{\sigma_{ij,j}}) - \underline{\sigma_{ij,j}} - f_i^{\mathrm{EXT,s}} \right] \mathrm{d}\Omega = 0. \tag{2}$$

The added terms in the modified equation above are underlined. One can easily determine that they sum to zero. This equation is rearranged so that the terms that have fluid properties can be grouped together to yield

$$\int_{\Omega^s} \delta v_i^s \left[(\rho^s - \rho) \frac{\mathrm{d}v_i^s}{\mathrm{d}t} - (\sigma_{ij,j}^s - \sigma_{ij,j}) - f_i^{\mathrm{EXT,s}} \right] \mathrm{d}\Omega + \underbrace{\int_{\bar{\Omega}} \delta v_i^s \left(\rho \frac{\mathrm{d}v_i^s}{\mathrm{d}t} - \sigma_{ij,j} \right) \mathrm{d}\Omega}_{\text{artificial fluid in } \Omega^s} = 0. \tag{3}$$

Eq. (3) now contains two terms. The first term is the work done by the solid in the solid domain subtracting the work done by the artificial fluid. The second term represents the work done by the artificial fluid in this overlapping domain. Notice that the equation is still in equilibrium.

We now define the interaction force as $f_i^{\mathrm{FSI}} = \rho(\mathrm{d}v_i/\mathrm{d}t) - \sigma_{ij,j}$, and express it in its weak form using the test function, δv_i,

$$\int_{\bar{\Omega}} \delta v_i \left(\rho \frac{\mathrm{d}v_i}{\mathrm{d}t} - \sigma_{ij,j} - f_i^{\mathrm{FSI}} \right) \mathrm{d}\Omega = 0. \tag{4}$$

Noting that since $\bar{\Omega}$ and Ω^s are equivalent, the integration domain in Eq. (4) is changed to $\bar{\Omega}$. The solid velocity $\mathbf{v}^s$ for the artificial fluid in the overlapping domain can be replaced by the fluid velocity $\mathbf{v}$ in Eq. (4), since they are identical in this domain based on the assumption of the no-slip boundary condition at the interface. Substituting Eq. (4) back into Eq. (3) and rearranging the terms, we obtain the following weak form for the solid in the overlapping domain,

$$\int_{\Omega^s} \delta v_i^s \left[(\rho^s - \rho) \frac{\mathrm{d}v_i^s}{\mathrm{d}t} - (\sigma_{ij,j}^s - \sigma_{ij,j}) - f_i^{\mathrm{EXT,s}} \right] \mathrm{d}\Omega = - \int_{\Omega^s} \delta v_i^s f_i^{\mathrm{FSI,s}} \, \mathrm{d}\Omega, \tag{5}$$

where $f_i^{\mathrm{FSI,s}}$ represents the interaction force acting on the solid.

Eqs. (4) and (5) complete the derivation for the governing equations of the solid and the artificial fluid. The next task is to combine the artificial fluid in $\bar{\Omega}$ described in Eq. (4) with the realistic or physical fluid in the fluid domain Ω^f, so that the fluid can be treated homogeneously in the entire computational domain Ω.

2.3. Fluid domain

The Navier-Stokes equations are used in the IFEM to describe a viscous Newtonian fluid. The variables are defined using an Eulerian description. Here, the fluid is considered to be incompressible. Both Neumann and Dirichlet types of boundaries can be applied at the fluid boundaries, though they may not overlap. The fluid domain, therefore, can be flexible in shape and size. It gives the advantage of modeling realistic fluid domains wherever necessary. The real fluid occupies the domain $\Omega^f \equiv \Omega \backslash \Omega^s$, i.e., the entire computational domain minus the solid domain. The continuity and momentum equations for the fluid in the fluid domain Ω^f are

$$v_{i,i} = 0, \tag{6a}$$

$$\rho(v_{i,t} + v_j v_{i,j}) = \sigma_{ij,j} + f_i^{\mathrm{EXT}}, \tag{6b}$$

where $\boldsymbol{\sigma}$ is the Cauchy stress which is a function of pressure and shear stress,

$$\sigma_{ij,j} = -p_{,i} + \mu(v_{i,jj} + v_{j,ij}). \tag{7}$$

If we assume that there is no external force applied to the fluid, i.e., $\mathbf{f}^{\mathrm{EXT}} = \mathbf{0}$, and express Eq. (6b) in its weak form using the test function, $\delta\mathbf{v}$, Eq. (6b) becomes

$$\int_{\Omega^f} \delta v_i [\rho(v_{i,t} + v_j v_{i,j}) - \sigma_{ij,j}] \, \mathrm{d}\Omega = 0. \tag{8}$$

Now, combining the work done by the real fluid in Eq. (8) and the artificial fluid described in Eq. (4) with the expansion of the total time derivative term, $\mathrm{d}v_i/\mathrm{d}t = v_{i,t} + v_j v_{i,j}$, we obtain

$$\underbrace{\int_{\tilde{\Omega}} \delta v_i[\rho(v_{i,t} + v_j v_{i,j}) - \sigma_{ij,j} - f_i^{\mathrm{FSI}}]\,\mathrm{d}\Omega}_{\text{artificial fluid in the overlapping domain, } \tilde{\Omega}, \text{ Eq. (4)}} + \underbrace{\int_{\Omega^{\mathrm{f}}} \delta v_i[\rho(v_{i,t} + v_j v_{i,j}) - \sigma_{ij,j}]\,\mathrm{d}\Omega}_{\text{real fluid in the fluid domain, } \Omega^{\mathrm{f}}, \text{ Eq. (8)}} = 0. \tag{9}$$

The first integrand in Eq. (9) is the same as the momentum equation of the Navier–Stokes equation, except for the existence of the term f_i^{FSI}. This interaction force only exists in the overlapping region and its immediate surrounding. Its value diminishes to zero at places outside the region (we will show details in the following section). Therefore, the two integral terms in Eq. (9) can be combined into the entire computational domain, Ω, as

$$\int_{\Omega} \delta v_i[\rho(v_{i,t} + v_j v_{i,j}) - \sigma_{ij,j} - f_i^{\mathrm{FSI}}]\,\mathrm{d}\Omega = 0. \tag{10}$$

Since the fluid is homogenous and both physical and artificial fluids are assumed to be incompressible, we can write the complete governing equations of the fluid as

$$v_{i,i} = 0, \tag{11a}$$

$$\rho(v_{i,t} + v_j v_{i,j}) - \sigma_{ij,j} - f_i^{\mathrm{FSI}} = 0. \tag{11b}$$

The only deviation of Eq. (11) from the conventional Navier–Stokes equation is the term f_i^{FSI}. In the IFEM formulation, this term can be interpreted as the external force applied to the fluid that is generated from the artificial fluid. The details of the discretization process for the above equations can be found in Zhang et al. (2004).

2.4. Solid domain

We first make two assumptions before proceeding to the descriptions of the solid domain. First, the solid must always remain immersed in the fluid domain throughout each simulation. If the solid falls out of the fluid domain, the interactions between the fluid and the solid are not guaranteed to be interpolated correctly at the interface, which will be shown in the following section. Second, the solid has to be an incompressible material or at least a nearly-incompressible material. Since the previous assumption states that the solid is completely immersed in the fluid and the fluid is assumed to be incompressible, the solid must maintain the same constraint as the fluid. If the volume of the solid changes, it forces the fluid volume to be changed as well. This, in turn, contradicts the assumption made, although it would not be influential if the volume of the solid is significantly smaller than that of the fluid.

Both Neumann and Dirichlet boundaries can be applied at the solid boundaries. Therefore, external forces acting on the solid, $\mathbf{f}^{\mathrm{EXT,s}}$, such as gravity, can be easily implemented. The governing equation for the solid was derived in Eq. (5). The solid is described using a Lagrangian formulation. A transformation is needed to convert the variables from the current configuration or updated Lagrangian formulation, Ω^{s}, to total Lagrangian formulation, Ω_0^{s}. The Cauchy stress $\boldsymbol{\sigma}$ can be derived from the first Piola-Kirchhoff stress, $\mathbf{P}$, which is determined by the material types and properties. Transformations between stresses can be found in Belytschko et al. (2000). With $\mathrm{d}v_i^{\mathrm{s}}/\mathrm{d}t = \ddot{u}_i^{\mathrm{s}}$, Eq. (5) becomes

$$\int_{\Omega_0^{\mathrm{s}}} \delta u_i^{\mathrm{s}}[(\rho^{\mathrm{s}} - \rho)\ddot{u}_i^{\mathrm{s}} - (P_{ij,j}^{\mathrm{s}} - P_{ij,j}) - f_i^{\mathrm{EXT,s}}]\,\mathrm{d}\Omega = -\int_{\Omega_0^{\mathrm{s}}} \delta u_i^{\mathrm{s}} f_i^{\mathrm{FSI,s}}\,\mathrm{d}\Omega, \tag{12}$$

or its strong form,

$$(\rho^{\mathrm{s}} - \rho)\ddot{u}_i^{\mathrm{s}} - (P_{ij,j}^{\mathrm{s}} - P_{ij,j}) - f_i^{\mathrm{EXT,s}} = -f_i^{\mathrm{FSI,s}}. \tag{13}$$

Material descriptions determine the stress calculations in Eq. (13). Two types of materials are implemented in the current IFEM: nearly-incompressible hyperelastic material and incompressible elastic material. We first consider an almost incompressible hyperelastic material model with a Mooney-Rivlin material description (Wang and Liu, 2004), in which the strain energy function W is given as

$$W = C_1(J_1 - 3) + C_2(J_2 - 3) + \frac{\kappa}{2}(J_3 - 1)^2, \tag{14}$$

where C_1, C_2, and κ are the material constants and J_1, J_2, and J_3 are functions of the invariants of the Cauchy-Green deformation tensor $\mathbf{C}$ defined as $C_{ij} = F_{im}F_{jm}$.

For structures with large displacements and deformations, the second Piola-Kirchhoff stress S_{ij} and the Green-Lagrangian strain E_{ij} are used:

$$S_{ij} = \frac{\partial W}{\partial E_{ij}} \quad \text{and} \quad E_{ij} = \frac{1}{2}(C_{ij} - \delta_{ij}). \tag{15}$$

The first Piola-Kirchhoff stress P_{ij} can then be obtained from the second Piola-Kirchhoff stress S_{ij} using $P_{ij} = S_{ik}F_{jk}$.

The second material type to be considered is an incompressible elastic material where Hooke's law is used. The generalized Hooke's law for a two-dimensional plane stress elastic material can be written as

$$\sigma_{11} = \frac{E}{1-v^2}(E_{11} + vE_{22}), \quad \sigma_{22} = \frac{E}{1-v^2}(E_{22} + vE_{11}), \quad \sigma_{12} = \frac{E}{1+v}E_{12} = \sigma_{21}, \tag{16a,b,c}$$

where E is Young's modulus and v is Poisson ratio. The first Piola-Kirchhoff stress tensor can be computed using $P_{ij} = JF^{-1}_{ik}\sigma_{kj}$, where F_{ik} is the deformation gradient and J is its determinant.

2.5. Interpolations between fluid and solid domains

The solid and fluid meshes are constructed independently in order to avoid frequent mesh updating. By taking advantage of the assumption of the no-slip boundary condition applied at the interface Γ^{FSI} or Γ^{s}, the solid can maintain the same velocity as its surrounding fluid. With the two independent meshes, however, it is nearly impossible to have the moving solid boundary nodes on Γ^{s} coinciding with the nodes in Ω at each time step. An interpolation function must be used to couple the fluid grid velocity $\mathbf{v}(\mathbf{x}, t)$ and the solid nodal velocity $\mathbf{v}^{\mathrm{s}}(\mathbf{X}^{\mathrm{s}}, t)$ within the overlapping domain. The solid nodal positions are then updated based on the interpolated velocity field. Likewise, the interaction force $\mathbf{f}^{\mathrm{FSI,s}}(\mathbf{X}^{\mathrm{s}}, t)$ calculated from the solid equation, Eq. (13), is distributed onto the nodes in the fluid domain $\mathbf{f}^{\mathrm{FSI}}(\mathbf{x}, t)$. To obtain accurate interpolations, a high-order interpolation function should be adopted.

2.5.1. The delta function

In this section we describe in detail the construction of the delta function, δ, which is used as the interpolation function. Peskin (2002) used a Dirac delta function for the interpolations, which is a C^1 order function and is suitable for uniform fluid grids. If the fluid domain is discretized with nonuniform grids, however, this particular Dirac delta function can no longer be valid. Instead, a more generalized delta function that satisfies the consistency condition must be acquired. In the IFEM, we employ the interpolation function used in Reproducing Kernel Particle Method (RKPM) (Liu et al., 1995; Li and Liu, 2002; Kim et al., 2003; Wang and Liu, 2004). As illustrated in Liu et al. (1995), both wavelet and smooth particle hydrodynamics (SPH) methods belong to a class of reproducing kernel methods where the reproduced function $u^{\mathrm{R}}(x)$ is derived as

$$u^{\mathrm{R}}(x) = \int_{-\infty}^{+\infty} u(y)\phi(x-y)\,\mathrm{d}y, \tag{17}$$

with a projection operator or a window function $\phi(x)$.

The reproducing condition requires that up to nth order polynomial can be reproduced, i.e.,

$$x^n = \int_{-\infty}^{+\infty} y^n \phi(x-y)\,\mathrm{d}y. \tag{18}$$

To satisfy the consistency condition, a correction function $C(x; x-y)$ is introduced in the finite domain of influence or support, so that the window function yields

$$\int_{\Omega} C(x; x-y)\frac{1}{a}\phi\left(\frac{x-y}{a}\right)\mathrm{d}\Omega = 1, \tag{19}$$

where a is the dilation parameter or refinement of the window function. The additional constant, a^{-1}, scales the window function so that the integral over the domain of support equals one. The discretized reconstruction of the delta function can be written as

$$\phi_I(x) = C(x; x-y)\frac{1}{a}\phi\left(\frac{x-y}{a}\right)\Delta y. \tag{20}$$

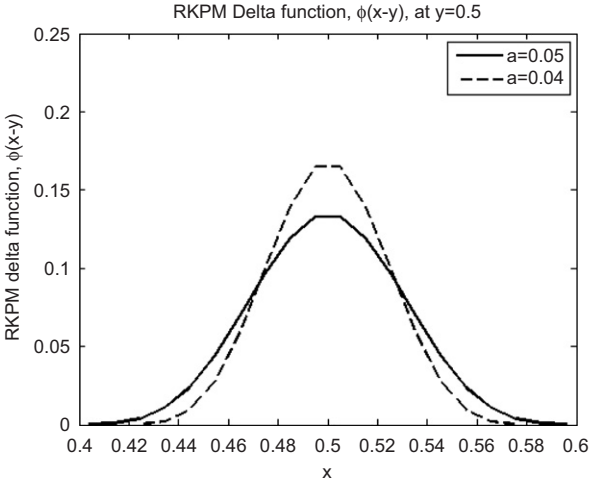

Fig. 2. RKPM delta function for dilation parameters $a = 0.04$ and $a = 0.05$.

A comparison between different dilation parameters ($a = 0.04$ and $a = 0.05$) used in the delta function is shown in Fig. 2. The window function, ϕ, used here is a cubic spline. The discretized delta function values are evaluated at $y = 0.5$ in $\mathbf{x} = [0, 1]$. It clearly shows that the dilation parameter controls the size of the supporting domain or the influence domain. The supporting domain enlarges as the dilation parameter increases. The RKPM delta function distribution, $\phi_I(x)$, is also compared for uniform (Fig. 3(a)) and nonuniform meshes (Fig. 3(b)) in a 1-D domain $\mathbf{x} = [0, 1]$ at $y = 0.5$. The nonuniform mesh is generated by randomly positioned nodes. The weight of each node (i.e., the distance between the neighboring node) is also plotted. Fig. 3(b) exemplifies a "nonsmooth" delta function distribution which is due to the nonuniformity. The sizes of the supporting domains, however, are the same for both cases when the same a is used. If the window function is chosen to be a second order polynomial, then the RKPM interpolation function can be reduced to the Dirac delta function if uniform grid is used.

2.5.2. *Velocity interpolation and force distribution*

Because of its higher order accuracy and its ability in handling nonuniform meshes, this RKPM shape function is used as the delta function to interpolate nodal velocities and nodal forces between the fluid and the solid domains. To ensure conservation of energy, the delta functions used in both distribution and interpolation procedures must be the same (Peskin, 2002).

The velocity interpolation in discretized form is written as

$$v_{iI}^{s} = \sum_{J} v_{iJ}(t)\phi_J(\mathbf{x}_J - \mathbf{x}_I^{s}), \quad \mathbf{x}_J \in \Omega_{\phi I}. \tag{21}$$

Here, the solid velocity $\mathbf{v}_I^{s}$ at node I can be calculated by gathering the velocities of its surrounding fluid nodes that fall within the influence domain $\Omega_{\phi I}$; ϕ is the interpolation function that we defined previously for nonuniform fluid grid. All the variables used in Eq. (21) are illustrated in Fig. 4. In particular, for each solid node I at its current position $\mathbf{x}_I^{s}(t)$, we construct an influence domain $\Omega_{\phi I}$ that covers a subset of the fluid grid nodes J positioned at $\mathbf{x}_J$. To define the influence domain for each solid point I, a search algorithm within the entire fluid domain Ω^{f} is performed at each time step for calculating the RKPM delta functions Eq. (20). By interpolating the fluid velocities onto the solid particles using Eq. (21), the artificial fluid is bounded to the solid domain. This not only ensures the no-slip boundary condition on the surface of the solid, but also automatically stops the fluid from penetrating into the solid region.

A dual procedure takes place when distributing the interaction force from the solid onto the fluid. A fluid node J at position $\mathbf{x}_J$ may fall into one or more influence domains $\Omega_{\phi I}$ of the surrounding solid nodes ($\mathbf{x}_I^{s}$), as shown in Fig. 5. Therefore, the interaction force calculated at each solid node contributes to a portion of the force at each surrounding fluid node. The distribution function can be expressed in the discretized form as

$$f_{iJ}^{FSI} = \sum_{I} f_{iI}^{FSI,s}(\mathbf{X}^{s}, t)\phi_I(\mathbf{x}_J - \mathbf{x}_I^{s}), \quad \mathbf{x}_I^{s} \in \Omega_{\phi J}. \tag{22}$$

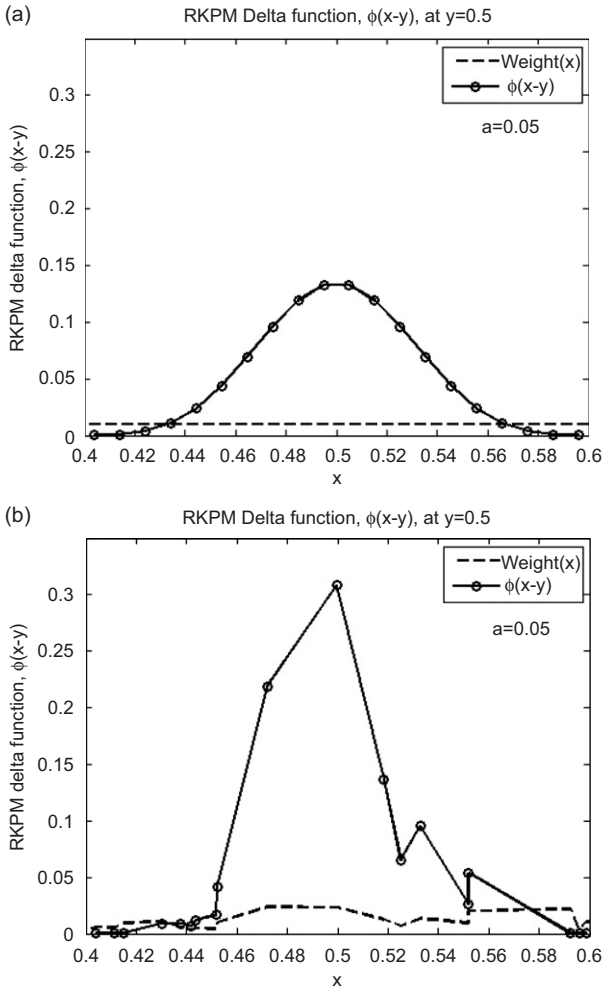

Fig. 3. RKPM delta function for (a) uniform grid and (b) nonuniform grid.

2.6. Summary

This section summarizes the entire algorithm along with the assumptions made throughout the derivation. The assumptions are: (i) the fluid is incompressible; (ii) the solid is an incompressible or nearly incompressible material; (iii) the solid must remain completely immersed in the fluid throughout the simulation; and (iv) no-slip boundary condition is applied at the fluid-structure interface.

Finally, with the variables in the solid domain Ω^s defined using a Lagrangian description and the fluid domain Ω using an Eulerian description, we can summarize the governing equations as well as the interpolation and distribution processes as follows:

$$f_i^{\mathrm{FSI,s}} = -(\rho^s - \rho)\ddot{u}_i^s + \sigma_{ij,j}^s - \sigma_{ij,j} + (\rho^s - \rho)g_i, \quad \text{in } \Omega^s, \tag{23a}$$

$$f_i^{\mathrm{FSI}}(\mathbf{x}, t) = \int_{\Omega^s} f_i^{\mathrm{FSI,s}}(\mathbf{X}^s, t)\phi(\mathbf{x} - \mathbf{x}^s(\mathbf{X}^s, t))\,\mathrm{d}\Omega, \tag{23b}$$

$$\rho(v_{i,t} + v_j v_{i,j}) = \sigma_{ij,j} + f_i^{\mathrm{FSI}}, \quad \text{in } \Omega, \tag{23c}$$

$$v_{i,i} = 0, \quad \text{in } \Omega, \tag{23d}$$

$$v_i^s(\mathbf{X}^s, t) = \int_{\Omega} v_i(\mathbf{x}, t)\phi(\mathbf{x} - \mathbf{x}^s(\mathbf{X}^s, t))\,\mathrm{d}\Omega, \tag{23e}$$

$$u_i^{s,n+1} = v_i^{s,n+1}\Delta t. \tag{23f}$$

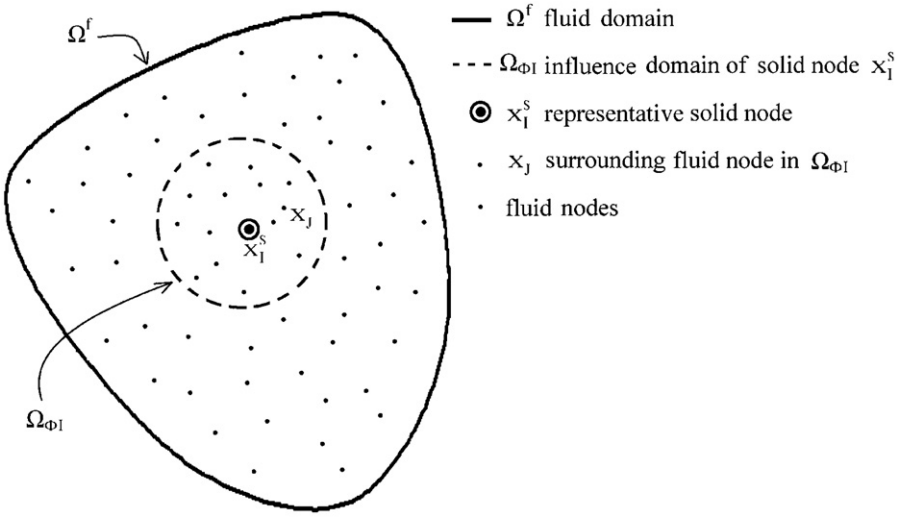

Fig. 4. Definitions used in velocity interpolation process.

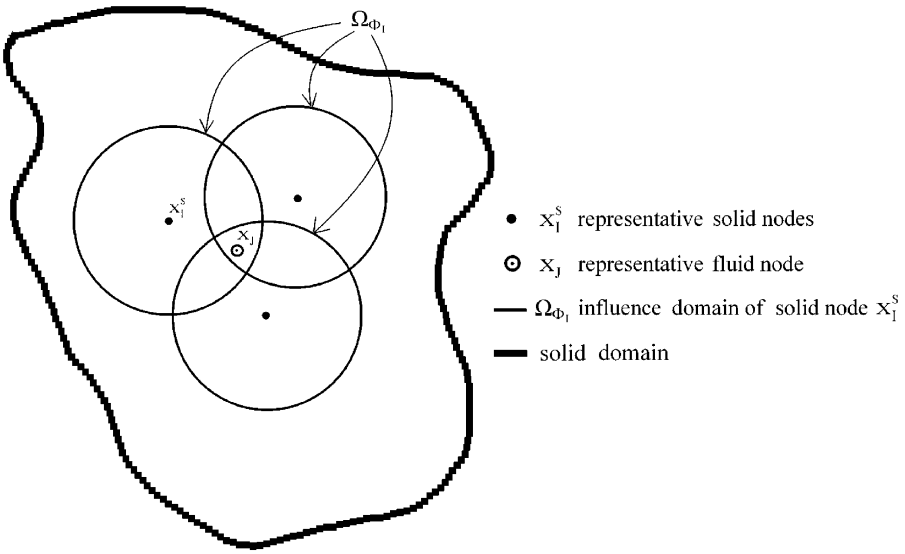

Fig. 5. Definitions used in force distribution process.

An outline of the IFEM algorithm with a semi-explicit time integration is illustrated as follows:

(1) given the structural configuration $\mathbf{x}^{s,n}$ and the fluid velocity $\mathbf{v}^n$ at time step n,
(2) evaluate the nodal interaction forces $\mathbf{f}^{FSI,s,n}$ at solid material points, using Eq. (23a),
(3) distribute the material nodal force onto the fluid lattice, from $\mathbf{f}^{FSI,s,n}$ to $\mathbf{f}^{FSI,n}$ using delta function Eq. (23b),
(4) solve for fluid velocities $\mathbf{v}^{n+1}$ and pressure $\mathbf{p}^{n+1}$ implicitly using Eqs. (23c) and (23d),
(5) interpolate the velocities in the fluid domain to the material points, i.e., from $\mathbf{v}^{n+1}$ to $\mathbf{v}^{s,n+1}$ as in Eq. (23e), and
(6) update the positions of the solid using Eq. (23f), then go back to step 1.

Remarks

(i) Unlike conventional solid solvers which have the displacement field as the unknown, the IFEM solid equation has the interaction force, $\mathbf{f}^{FSI}$, as the unknown and the displacement is updated through the interpolation of the fluid

velocity. The Navier–Stokes equations can be solved as usual, where the variables of interest are pressure **p** and velocity **v**.

(ii) This straightforward algorithm can be easily implemented. One who possesses a fluid code and a solid code can simply combine them and solve fluid-structure interaction types of problems. The interpolation and distribution processes are the only additional algorithms that need to be implemented.

(iii) With appropriate adjustments in the governing equations, this IFEM concept can be applied to other types of interaction problems as well, such as multiphase flows.

(iv) Based on a number of numerical tests, the fluid grid spacing has to be approximately twice that of the solid to avoid fluid sinking through into the solid domain (Gay et al., 2006). Although this criterion need not to be followed as an exact measure since grids are not required to be uniformly spaced, a general rule of thumb is to keep the fluid grid spacing larger, but not so large as it may decrease the accuracy.

(v) Even though the fluid domain itself can be solved implicitly, the interpolation of the velocities and the distribution of the forces are performed explicitly using the delta function. This restricts the time step size involved in the simulations. Consequently, as the solid material gets more rigid, the time step has to be smaller. Thus, a fully implicit version of this algorithm has been developed (Wang, 2006); but it is a compromise between small time steps and increased number of convergence iterations at each step.

3. Numerical examples

In this section, two numerical examples are investigated to validate the computational algorithm. The first example studies the motion of a soft disk falling in a viscous fluid. The second example studies the motion of a two-dimensional leaflet under various sinusoidal fluid flow conditions.

Table 1
Fluid and material properties and dimensions used in Example 1 (disk falling in a channel)

Fluid domain	Soft disk
$W = 2.0\,\text{cm}$	$d = 0.5\,\text{cm}$
$H = 5.0\,\text{cm}$	$\rho^s = 3.0\,\text{g/cm}^3$
$\rho = 1.0\,\text{g/cm}^3$	$E = 10\,000\,\text{dyne/cm}^2$
$\mu = 1.0\,\text{dyne/cm}^2\,\text{s}$	$v = 0.3$

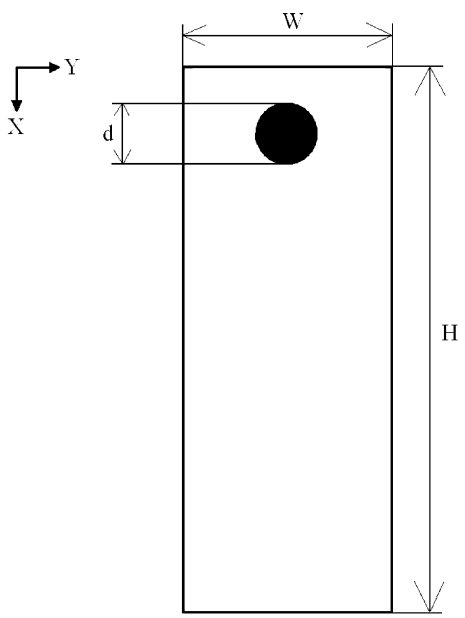

Fig. 6. A soft disk falling in a channel.

3.1. A soft disk falling in a viscous fluid

We study the motion of a soft disk falling in an incompressible viscous fluid due to gravity. Using this simple verification problem we shall draw a detailed overview diagram to illustrate how the IFEM algorithm proceeds from one step to another in both fluid and solid domains.

3.1.1. Problem description

We consider a 2-D soft (deformable) disk of diameter $d = 0.5\,\text{cm}$ located in a 2-D channel of width $W = 2.0\,\text{cm}$. The disk is described using an elastic model with Young's modulus $E = 10^4\,\text{dyne/cm}^2$, Poisson ratio $v = 0.3$ and density $\rho^s = 3.0\,\text{g/cm}^3$. This deformable disk is fully immersed in a Newtonian incompressible viscous fluid with density $\rho = 1.0\,\text{g/cm}^3$ and viscosity $\mu = 1.0\,\text{dyne/cm}^2\,\text{s}$. The defined parameters and material properties are summarized in Table 1. Initially, the disk is placed at the top of the fluid domain and both the disk and the fluid are at rest, i.e., $\mathbf{v} = \mathbf{0}$ and $\mathbf{v}^s = \mathbf{0}$ at $t = 0$, as shown in Fig. 6. Quadrilateral elements are used to discretized both fluid and solid computational domains. The disk has 414 elements and 447 nodes and the fluid domain 2000 elements and 2121 nodes.

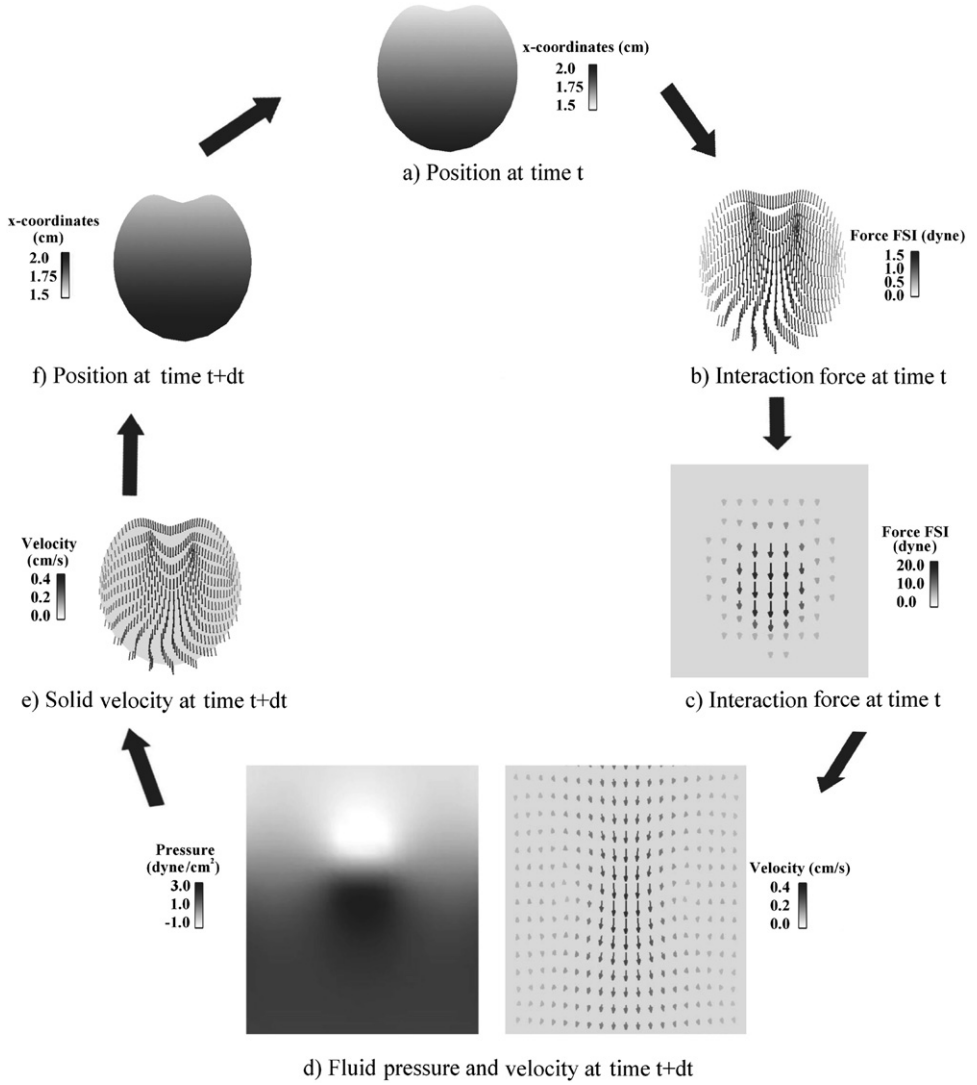

Fig. 7. Steps of the IFEM algorithm.

3.1.2. Illustrative description of the IFEM algorithm

Fig. 7 shows in detail the computational steps of the IFEM outlined in Section 2. Fig. 7(a) shows the solid configuration at time t. The nodal interaction forces for the solid material points are then computed as shown in Fig. 7(b) using Eq. (23a). These interaction forces are distributed onto the surrounding fluid (Fig. 7(c)) using Eq. (23b). Velocity and pressure (Fig. 7(d)) are solved using the Navier-Stokes equations at the following time step $t + \Delta t$ using Eq. (23c) and Eq. (23d). Using the velocity interpolation function detailed previously in Eq. (23e), the fluid velocity is interpolated onto the solid nodes (Fig. 7(e)). Finally, the solid displacement and new configuration can be updated with the interpolated velocity using Eq. (23f), as shown in Fig. 7(f). This process is then repeated for the next time step.

3.1.3. Results and discussion

Due to the effect of gravity, the disk accelerates downward and eventually reaches its terminal velocity. A small Reynolds number is assumed; therefore, the tube is large enough compared to the disk size to ignore the wall effects. The deformation of the disk is symmetric, as expected, and is due to the viscous effect along the interfacial boundaries. Fluid recirculations are generated along the fluid-structure interface, which correspond directly to the deformation of the disk. The fluid recirculation and the solid deformation at different time steps are shown in Fig. 8.

For a very flexible object moving in a viscous environment, the proposed IFEM algorithm can capture both the normal and shear stress distributions of the moving solid at different time steps. The normal (σ_{xx} and σ_{yy}) and shear (σ_{xy}) stress distributions are presented in Fig. 9. Comparing with the normal stress, this moving deformable disk experiences a significant shear.

In order to determine the accuracy of the IFEM, we compare the terminal velocity of the disk with an empirical solution of a rigid disk falling in viscous fluid (Clift et al., 1978). The terminal settling velocity u_t of a rigid disk under gravity is given by

$$u_t = \frac{(\rho^s - \rho)gr^2}{4\mu}\left(\ln\left(\frac{L}{r}\right) - 0.9157 + 1.7244\left(\frac{r}{L}\right)^2 - 1.7302\left(\frac{r}{L}\right)^4\right), \tag{24}$$

where r is the radius of the disk and L is half the width of the fluid domain ($L = W/2$). Fig. 10 compares the velocity history of the deformable disk and the terminal velocity of the rigid sphere. This clearly shows that the deformation of the solid structure has an effect on the terminal velocity. The flexibility of the disk decreases the surrounding fluid force

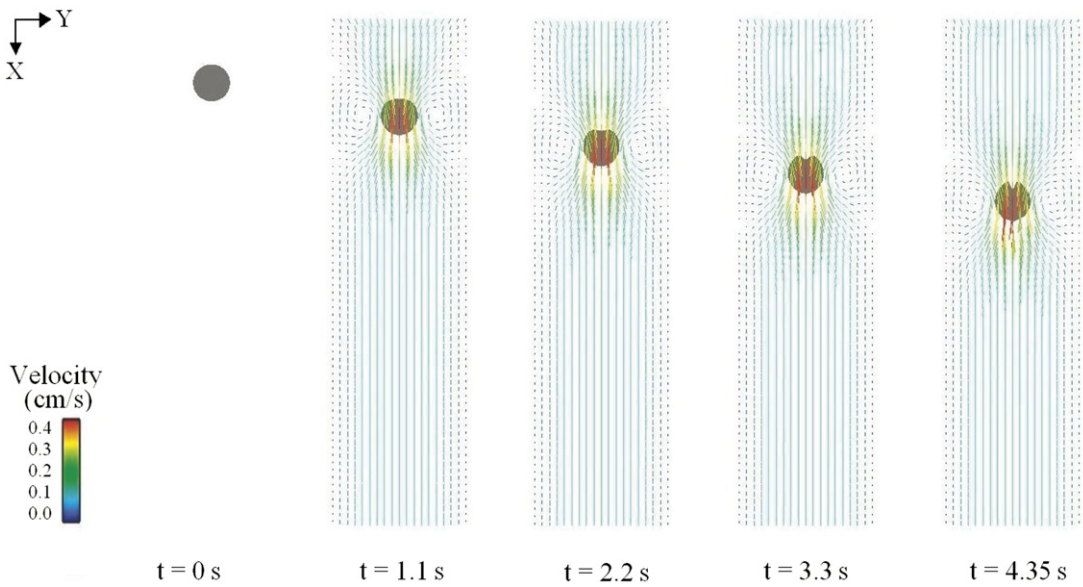

Fig. 8. Fluid velocity field and disk deformation at different time steps.

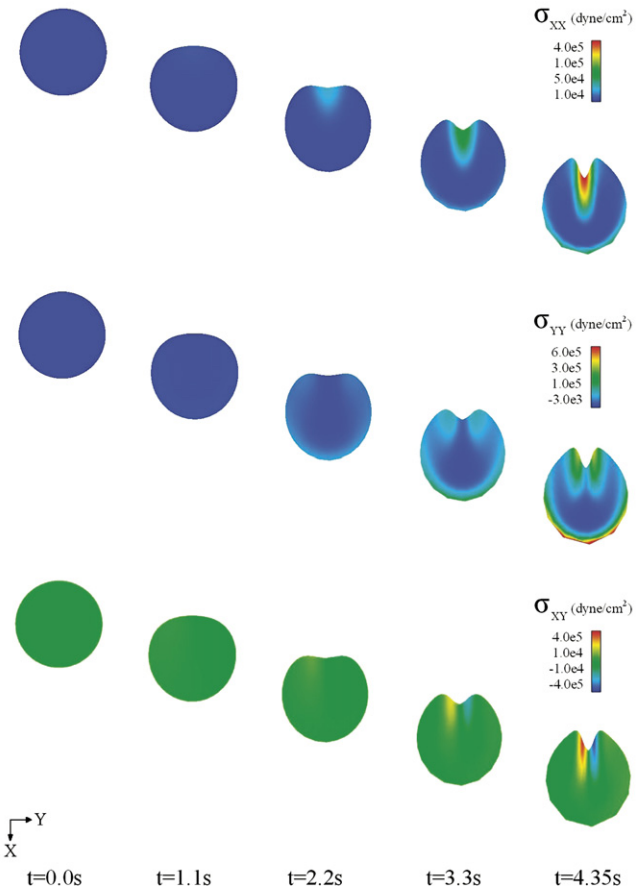

Fig. 9. Stress distributions on the soft disk at different time steps.

(viscous shear), thus increases the magnitude of the terminal velocity. The Reynolds number for a disk in a viscous fluid is defined as

$$\mathrm{Re} = \frac{\rho u_t d}{\mu}. \tag{25}$$

Thus, a corresponding Reynolds number of $\mathrm{Re} = 0.2$ is reached in this simulation, which validates the assumption of small Reynolds number made initially to avoid wall effects during the falling of the disk.

3.2. *Leaflet driven by a sinusoidal fluid flow*

This example analyzes large, complex, and time-dependent deflections of a thin flexible body driven by viscous fluid flows with time-varying inflow boundary conditions. This type of problem is of great importance in solving realistic biomechanical problems, such as the opening and closing behavior of aortic heart valves, which involve delicate interactions between blood flow and heart-valve leaflets (de Hart et al., 1998).

3.2.1. *Problem description*

The leaflet investigated in this section is a thin two-dimensional rectangular shaped solid with length $\lambda = 0.8\,\mathrm{cm}$ and width $t = 0.0212\,\mathrm{cm}$ immersed in a 2-D rectangular fluid domain of size $H = 1.0\,\mathrm{cm}$ and $L = 4.0\,\mathrm{cm}$. The leaflet is assumed to be linear elastic with Young's modulus $E = 10^7\,\mathrm{dyne/cm^2}$, Poisson ratio $v = 0.5$, and density $\rho^s = 6.0\,\mathrm{g/cm^3}$. The Newtonian incompressible viscous fluid has density $\rho = 1.0\,\mathrm{g/cm^3}$ and viscosity $\mu = 0.1\,\mathrm{dyne/cm^2\,s}$. The material properties and parameters used in this example are summarized in Table 2. The

leaflet structure is fixed at one end at the mid-length of the fluid domain. This fixed boundary condition is enforced by connecting a series of tether points to the fixed points (Arthurs et al., 1998; Dillon et al., 1996). Initially, the leaflet is at rest, i.e., $\mathbf{v}^s = \mathbf{0}$ at $t = 0$. A sinusoidal input velocity $U_{in} = \sin(\pi t + \pi/2)$ with an amplitude of 1 cm/s and period of $\tau = 2$ s is applied at $y = 0$ and $y = L$, the bottom and top of the fluid domain, respectively. The no-slip boundary condition is applied along the right side of the fluid domain, i.e., $\mathbf{v}^s = \mathbf{0}$ on $x = H$. Along the left side of the fluid domain, the velocity in the horizontal direction is set to zero, i.e., $v_x = 0$, to represent a symmetry condition. Geometrical parameters and the input fluid velocity profile are shown in Fig. 11. Quadrilateral elements are used to discretize both fluid and solid computational domains. The solid structure has 456 elements and 575 nodes and the fluid domain 2500 elements and 2626 nodes.

3.2.2. Results and discussion

The motion of the leaflet is examined at different Strouhal (St) and Reynolds (Re) numbers. They are defined as follows:

$$\mathrm{St} = \frac{H}{U\tau} \quad \text{and} \quad \mathrm{Re} = \frac{\rho U H}{\mu}, \tag{26}$$

where U is the characteristic velocity (mean velocity), H is the characteristic length (channel height), and τ is a characteristic time (period). Fig. 12 shows the leaflet motion and velocity profile at different time steps for $\mathrm{Re} = 1.0$ and $\mathrm{St} = 1.0$. Starting from its initial position, the leaflet tip is pushed upward and the body tilted along with the direction of the flow until the flow velocity reaches its maximum. As soon as the flow starts to decrease, the leaflet flexes back due to its elastic property. Once the flow reverses its direction, the leaflet accelerates again, and eventually reaches a fully deflected configuration when the flow reaches its maximum in the opposite direction. This pattern repeats itself for every period. The leaflet motion follows the same behavior as the ones obtained from Baaijens (2001) and Yu (2005) using the

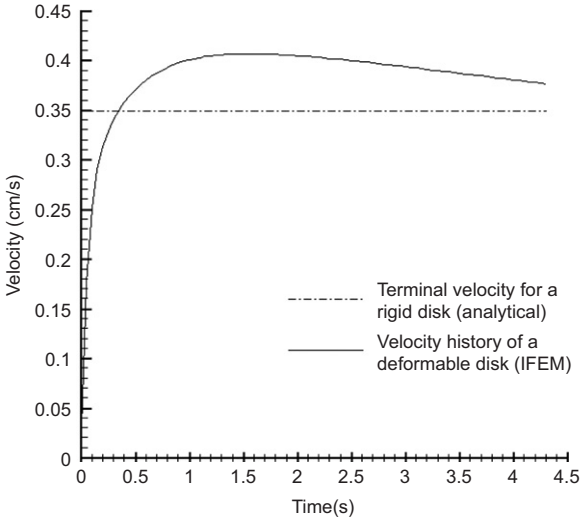

Fig. 10. Terminal velocity comparisons between a soft and a rigid disk falling in a channel.

Table 2
Fluid and material properties and dimensions used in Example 2 (leaflet in a channel)

Fluid domain	Leaflet
$H = 1.0$ cm	$\lambda = 0.8$ cm
$L = 4.0$ cm	$t = 0.0212$ cm
$\rho = 1.0$ g/cm^3	$\rho^s = 6.0$ g/cm^3
$\mu = 0.1$ dyne/cm^2 s	$E = 10^7$ dyne/cm^2
	$v = 0.5$

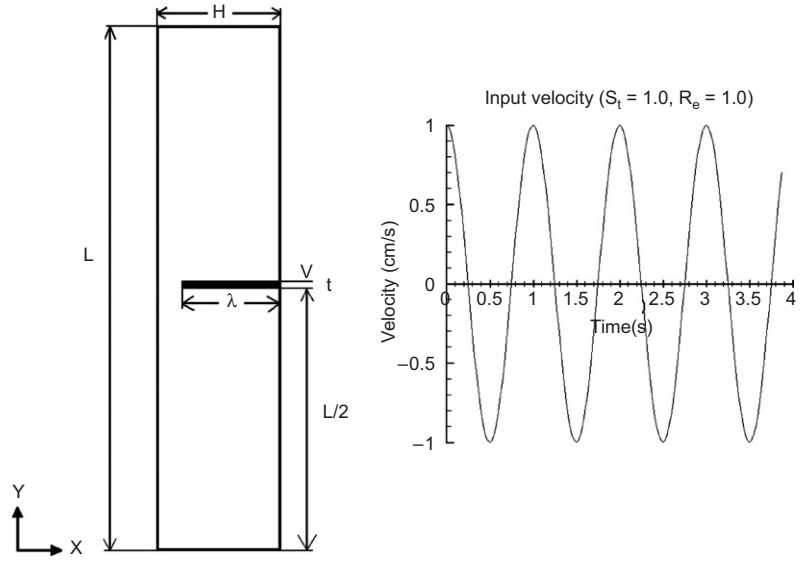

Fig. 11. A leaflet with one fixed-end in a channel and input fluid velocity profile at $y = 0$.

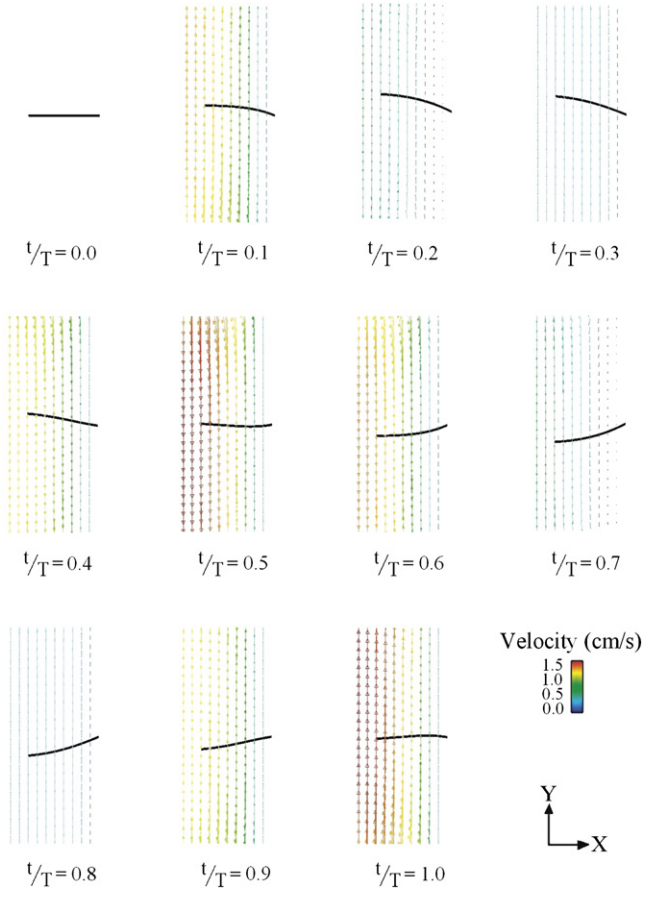

Fig. 12. Leaflet motion and fluid velocity profile (Re = 1.0 and St = 1.0) at different time steps.

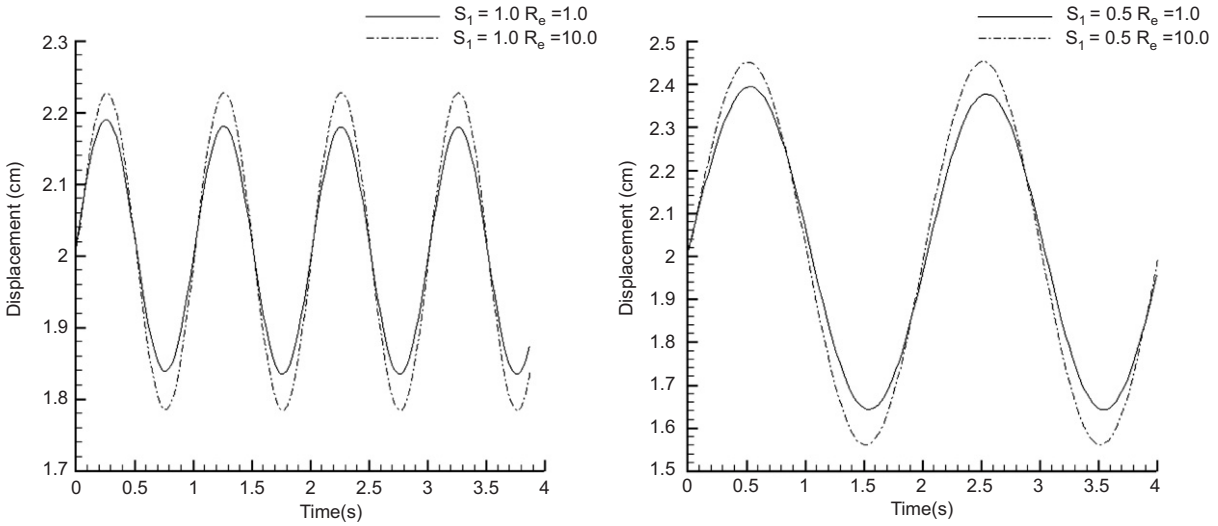

Fig. 13. Leaflet tip displacement at Reynolds numbers of 1.0 and 10.0 and Strouhal numbers of 1.0 and 0.5.

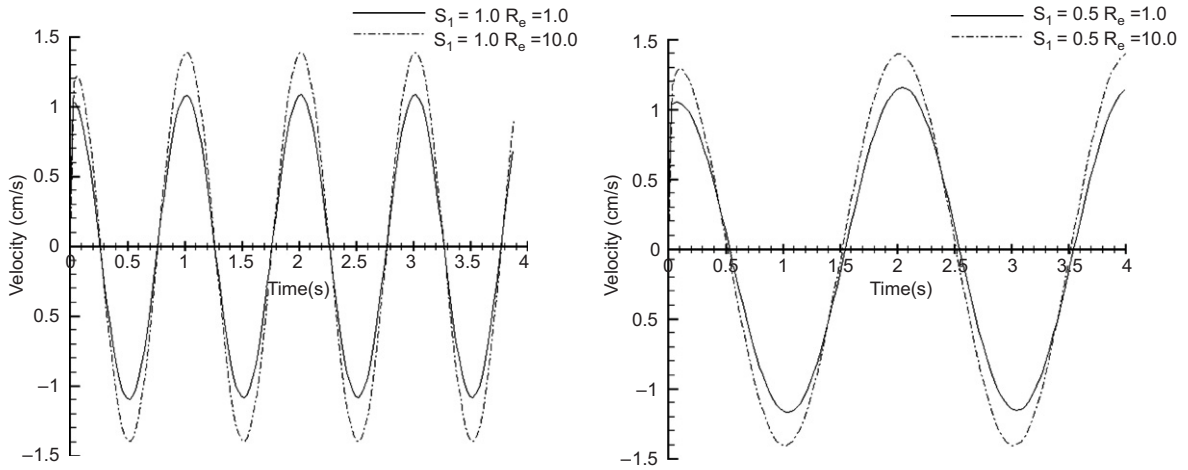

Fig. 14. Leaflet tip velocity at Reynolds numbers of 1.0 and 10.0 and Strouhal numbers of 1.0 and 0.5.

Fictitious Domain method. This sequence of movements clearly demonstrates the fluid-structure interaction capabilities of the IFEM. The effects of varying Strouhal and Reynolds numbers on the leaflet motion are shown in Figs. 13 and 14. Fig. 13 shows the tip displacements of the leaflet at Reynolds numbers of 1 and 10 and Strouhal numbers of 1 and 0.5. As the Reynolds number increases, the leaflet displacement and velocity increase. On the other hand, the Strouhal number does not affect the magnitude of the tip velocity of the leaflet, as shown in Fig. 14; it is only influenced by the Reynolds number. At higher Strouhal number ($St = 1.0$), the solid structure cannot reach a fully open position as it does for lower frequencies ($St = 0.5$) due to the lack of time needed for the leaflet to reach a maximum flexed position. Therefore, the maximum leaflet displacement at $St = 1.0$ is lower than the maximum displacement reached at $St = 0.5$.

4. Conclusions

In this paper, we derived in detail the Immersed Finite Element Method and showed its major advantageous features in solving complex fluid-structure interaction problems. With the use of a higher order interpolation function, both the

fluid and solid domains are capable of handling arbitrary geometries and boundary conditions. The IFEM is a major advancement in studying fluid-structure interactions, especially for immersed deformable objects. Detailed stress distributions, which are difficult to obtain experimentally or with the use of other computational methods, can now be analyzed using the IFEM.

Acknowledgement

The authors would like to thank the National Science Foundation (NSF) and NSF/EPSCoR programs (BOR RCS 545157) for their support.

References

Arthurs, K.M., Moore, L.C., Peskin, C.S., Pitman, E.B., Layton, H.E., 1998. Modeling arteriolar flow and mass transport using the immersed boundary method. Journal of Computational Physics 147, 402–440.

Baaijens, F.P.T., 2001. A fictitious domain/mortar element method for fluid–structure interaction. International Journal for Numerical Methods in Fluids 35, 743–761.

Belytschko, T., 1980. Fluid–structure interaction. Computers & Structures 12, 459–469.

Belytschko, T., Kennedy, J.M., 1976. A fluid–structure finite element method for the analysis of reactor safety problems. Nuclear Engineering and Design 38, 71–81.

Belytschko, T., Mullen, R., 1981. Two-dimensional fluid–structure impact computations with regularization. Computer Methods in Applied Mechanics and Engineering 27, 139–154.

Belytschko, T., Kennedy, J.M., Schoeberle, D.F., 1980. Quasi-Eulerian finite element formulation for fluid–structure interaction. ASME Journal of Pressure Vessel Technology 102, 62–69.

Belytschko, T., Liu, W.K., Moran, B., 2000. Nonlinear Finite Elements for Continua and Structures. Wiley, New York.

Chessa, J., Belytschko, T., 2003. The extended finite element method for two-phase fluids. Journal of Applied Mechanics 70, 10–17.

Chessa, J., Smolinski, P., Belytschko, T., 2002. The extended finite element method (XFEM) for solidification problems. International Journal for Numerical Methods in Engineering 53, 1959–1977.

Clift, R., Grace, J.R., Weber, M.E., 1978. Bubbles, Drops, and Particles. Academic Press, New York.

de Hart, J., Cacciola, G., Schreurs, P.J.G., Peters, G.W.M., 1998. A three-dimensional analysis of a fibre-reinforced aortic valve prosthesis. Journal of Biomechanics 31, 629–638.

Dillon, R., Fauci, L., Fogelson, A., Gaver III, D., 1996. Modeling biofilm processes using the immersed boundary method. Journal of Computational Physics 129, 57–73.

Fortin, M., Glowinski, R., 1983. Augmented Lagrangian Method: Applications to the Numerical Solution of Boundary-Value Problems. North-Holland, Amsterdam.

Gay, M., Zhang, L.T., Liu, W.K., 2006. Stent modeling using immersed finite element method. Computer Methods in Applied Mechanics and Engineering 195, 4358–4370.

Glowinski, R., Pan, T.W., Hesla, T.I., Joseph, D.D., 1999. A distributed Lagrange multiplier/fictitious domain method for particulate flows. International Journal of Multiphase Flow 25, 755–794.

Glowinski, R., Pan, T.W., Hesla, T.I., Joseph, D.D., Périaux, J., 2001. A fictitious domain approach to the direct numerical simulation of incompressible viscous flow past moving rigid bodies: application to particulate flow. Journal of Computational Physics 169, 363–426.

Hu, H.H., Patankar, N.A., Zhu, M.Y., 2001. Direct numerical simulations of fluid-solid systems using the arbitrary Lagrangian–Eulerian technique. Journal of Computational Physics 169, 427–462.

Huerta, A., Liu, W.K., 1988. Viscous flow with large free surface motion. Computer Methods in Applied Mechanics and Engineering 69, 277–324.

Hughes, T.J.R., Liu, W.K., Zimmermann, T.K., 1981. Lagrangian–Eulerian Finite Element formulation for incompressible viscous flows. Computer Methods in Applied Mechanics and Engineering 29, 329–349.

Johnson, A., Tezduyar, T., 1995. Numerical simulation of fluid-particle interactions. Proceedings of the International Conference on Finite Elements in Fluids, Venezia, Italy.

Johnson, A., Tezduyar, T., 1997. 3D simulations of fluid-particle interactions with the number of particles reaching 100. Computer Methods in Applied Mechanics and Engineering 145 (3–4), 301–321.

Johnson, A., Tezduyar, T., 1999. Advanced mesh generation and update methods for 3D flow simulations. Computational Mechanics 23, 130–143.

Kim, N.H., Choi, K.K., Botkin, M.E., 2003. Numerical method for shape optimization using a meshfree method. Structural and Multidisciplinary Optimization 24, 18–429.

Li, S., Liu, W.K., 1996. Moving least squares reproducing kernel method. Part II: Fourier analysis. Computer Methods in Applied Mechanics and Engineering 139, 159–194.

Li, S., Liu, W.K., 1999. Reproducing kernel hierarchical partition of unity. Part I: Formulation and theory. Computer Methods in Applied Mechanics and Engineering 145, 251–288.
Li, S., Liu, W.K., 2002. Meshfree and particle methods and their applications. Applied Mechanics Reviews 55, 1–34.
Li, S., Liu, W.K., 2004. Meshfree Particle Methods. Springer, 502pp.
Liu, W.K., 1981. Development of finite-element procedures for fluid–structure interaction. Ph.D. thesis, Pasadena, California.
Liu, W.K., Chen, Y.J., 1995. Wavelet and multiple scale reproducing kernel method. International Journal for Numerical Methods in Fluids 21, 901–932.
Liu, W.K., Ma, D.C., 1982. Computer implementation aspects for fluid–structure interaction problems. Computer Methods in Applied Mechanics and Engineering 31, 129–148.
Liu, Y., Liu, W.K., 2006. Rheology of red blood cell aggregation by computer simulation. Journal of Computational Physics 220, 139–154.
Liu, W.K., Belytschko, T., Chang, H., 1986. An arbitrary Lagrangian–Eulerian finite element method for path-dependent materials. Computer Methods in Applied Mechanics and Engineering 58, 227–245.
Liu, W.K., Chang, H., Chen, J., Belytschko, T., 1988. Arbitrary Lagrangian–Eulerian Petrov–Galerkin finite elements for nonlinear continua. Computer Methods in Applied Mechanics and Engineering 68, 259–310.
Liu, W.K., Jun, S., Zhang, Y.F., 1995. Reproducing kernel particle methods. International Journal for Numerical Methods in Fluids 20, 1081–1106.
Liu, W.K., Chen, Y., Chang, C.T., Belytschko, T., 1996a. Advances in multiple scale kernel particle methods. Computational Mechanics 18 (2), 73–111.
Liu, W.K., Chen, Y., Uras, R.A., Chang, C.T., 1996b. Generalized multiple scale reproducing kernel particle methods. Computer Methods in Applied Mechanics and Engineering 139, 91–158.
Liu, W.K., Liu, Y., Zhang, L.T., Wang, X., Gerstenberger, A., Farrell, D., 2004a. Immersed finite element method and applications to biological systems. Finite Element Methods: 1970's and Beyond. International Center for Numerical Methods and Engineering, 233–248.
Liu, Y., Zhang, L.T., Wang, X., Liu, W.K., 2004b. Coupling of Navier–Stokes equations with protein molecular dynamics and its application to hemodynamics. International Journal for Numerical Methods in Fluids 46 (12), 1237–1252.
Liu, W.K., Liu, Y., Farrell, D., Zhang, L.T., Wang, S., Fukui, Y., Patankar, N., Zhang, Y., Bajaj, C., Lee, J., Hong, J., Chen, X., Hsu, H., 2006. Immersed finite element method and its applications to biological systems. Computer Methods in Applied Mechanics and Engineering 195, 1722–1749.
McCracken, M.F., Peskin, C.S., 1980. A vortex method for blood flow through heart valves. Journal of Computational Physics 35, 183–205.
McQueen, D.M., Peskin, C.S., 1983. Computer-assisted design of pivoting-disc prosthetic mitral valves. Scandinavian Journal of Thoracic and Cardiovascular Surgery 86, 126–135.
McQueen, D.M., Peskin, C.S., 2001. Heart simulation by an Immersed Boundary method with formal second-order accuracy and reduced numerical viscosity. In: Aref, H., Phillips, J.W. (Eds.), Mechanics for a New Millennium, Proceedings of the International Conference on Theoretical and Applied Mechanics (ICTAM) 2000. Kluwer Academic Publishers, Dordrecht.
Peskin, C.S., 1972. Flow patterns around heart valves: A numerical method. Journal of Computational Physics 10, 252–270.
Peskin, C.S., 1977. Numerical analysis of blood flow in the heart. Journal of Computational Physics 25, 220–252.
Peskin, C.S., 2002. The immersed boundary method. Acta Numerica 11, 479–517.
Peskin, C.S., McQueen, D.M., 1989. A three-dimensional computational method for blood flow in the heart. I. Immersed elastic fibers in a viscous incompressible fluid. Journal of Computational Physics 81 (2), 372–405.
Peskin, C.S., McQueen, D.M., 1990. A heart valve prosthesis. European Patent Publication Number EP 0 211 576 B1.
Peskin, C.S., McQueen, D.M., 1991. Curved butterfly bileaflet prosthetic cardiac valve. U.S. Patent Number 5026391.
Peskin, C.S., McQueen, D.M., 1992. Cardiac fluid dynamics. Critical Reviews in Biomedical Engineering. SIAM Journal on Scientific and Statistical Computing 20 (6), 451–459.
Peskin, C.S., McQueen, D.M., 1993. Heart throb. Technical report. In Projects in Scientific Computing, a PSC Research Report.
Peskin, C.S., McQueen, D.M., 1994. Mechanical equilibrium determines the fractal fiber architecture of aortic heart valve leaflets. American Journal of Physiology 266 (1), H319–H328.
Peskin, C.S., McQueen, D.M., 1995. A general method for the computer simulation of biological systems interacting with fluids. Symposia of the Society for Experimental Biology Fluid Dynamics 49, 265–276.
Peskin, C.S., McQueen, D.M., 1996. Fluid dynamics of the heart and its valves. In: Othmer, H.G., Adler, F.R., Lewis, M.A., Dallon, J.C. (Eds.), Case Studies in Mathematical Modeling-Ecology, Physiology, and Cell Biology. Prentice-Hall.
Stein, K., Benney, R., Tezduyar, T., Potvin, J., 2001. Fluid–structure interactions of a cross parachute: numerical simulation. Computer Methods in Applied Mechanics and Engineering 191, 673–687.
Tezduyar, T., Behr, M., Liou, J., 1992. A new strategy for finite element computations involving moving boundaries and interfaces—The DSD/ST Procedure: I. The concept and the preliminary numerical tests. Computer Methods in Applied Mechanics and Engineering 94, 339–351.
Wagner, J., Moës, N., Liu, W.K., Belytschko, T., 2001. The extended finite element method for rigid particles in Stokes flow. International Journal for Numerical Methods in Engineering 51 (3), 293–313.
Wang, X., 2006. From immersed boundary method to immersed continuum method. International Journal for Multiscale Computational Engineering 1, 127–146.

Wang, X., Liu, W.K., 2004. Extended immersed boundary method using FEM and RKPM. Computer Methods in Applied Mechanics and Engineering 193, 1305–1321.

Yu, Z., 2005. A DLM/FD method for fluid/flexible-body interactions. Journal of Computational Physics 207, 1–27.

Zhang, L.T., Wagner, G.J., Liu, W.K., 2002. A parallized meshfree method with boundary enrichment for Large-Scale CFD. Journal of Computational Physics 176, 483–506.

Zhang, L.T., Wagner, G., Liu, W.K., 2003. Modeling and simulation of fluid structure interaction by meshfree and FEM. Communications in Numerical Methods in Engineering 19, 615–621.

Zhang, L.T., Gerstenberger, A., Wang, X., Liu, W.K., 2004. Immersed finite element method. Computer Methods in Applied Mechanics and Engineering 193, 2051–2067.